ELSEVIER

Contents lists available at ScienceDirect

Biosensors and Bioelectronics

journal homepage: www.elsevier.com/locate/bios



Miniaturized microarray-format digital ELISA enabled by lithographic protein patterning

Andrew D. Stephens^a, Yujing Song^a, Brandon L. McClellan^{b,c,d}, Shiuan-Haur Su^a, Sonnet Xu^a, Kevin Chen^e, Maria G. Castro^{b,c,f}, Benjamin H. Singer^{g,h}, Katsuo Kurabayashi^{i,*}

- ^a Department of Mechanical Engineering, University of Michigan, Ann Arbor, MI, 48109, USA
- ^b Department of Neurosurgery, University of Michigan Medical School, Ann Arbor, MI, 48109, USA
- ^c Department of Cell and Developmental Biology, University of Michigan Medical School, Ann Arbor, MI, 48109, USA
- ^d Graduate Program in Immunology, University of Michigan Medical School, Ann Arbor, MI, 48109, USA
- ^e Department of Biomedical Engineering, University of Michigan, Ann Arbor, MI, 48109, USA
- f Rogel Cancer Center, University of Michigan, Ann Arbor, MI, 48109, USA
- g Department of Internal Medicine, Division of Pulmonary and Critical Care Medicine, University of Michigan, Ann Arbor, MI, 48109, USA
- h Weil Institute for Critical Care Research and Innovation, University of Michigan, Ann Arbor, MI, 48109, USA
- ⁱ Department of Mechanical and Aerospace Engineering, New York University, Brooklyn, NY, 11201, USA

ARTICLE INFO

Keywords: Biomarker discovery Protein microarray Protein patterning Multiplex biomarker detection Digital immunoassay Glioma mouse model

ABSTRACT

The search for reliable protein biomarker candidates is critical for early disease detection and treatment. However, current immunoassay technologies are failing to meet increasing demands for sensitivity and multiplexing. Here, the authors have created a highly sensitive protein microarray using the principle of single-molecule counting for signal amplification, capable of simultaneously detecting a panel of cancer biomarkers at sub-pg/mL levels. To enable this amplification strategy, the authors introduce a novel method of protein patterning using photolithography to subdivide addressable arrays of capture antibody spots into hundreds of thousands of individual microwells. This allows for the total sensor area to be miniaturized, increasing the total possible multiplex capacity. With the immunoassay realized on a standard 75x25 mm form factor glass substrate, sample volume consumption is minimized to $<10~\mu$ L, making the technology highly efficient and cost-effective. Additionally, the authors demonstrate the power of their technology by measuring six secretory factors related to glioma tumor progression in a cohort of mice. This highly sensitive, sample-sparing multiplex immunoassay paves the way for researchers to track changes in protein profiles over time, leading to earlier disease detection and discovery of more effective treatment using animal models.

1. Introduction

Unlocking the potential of protein biomarkers in blood and other bodily fluids is essential for the diagnosis, prognosis, and treatment of many diseases including cancer (Borrebaeck, 2018) neurological disorders (Zetterberg and Blennow, 2020), immune dysfunction (Sarma et al., 2020), and cardiac injury (Park et al., 2017). However, current analytical techniques are technologically limited in identifying reliable protein biomarkers in the vast human proteome (Waury et al., 2022). Biomarker discovery typically begins with untargeted approaches, commonly mass spectrometry or transcriptomic analysis, generating large lists of potential candidates related to the disease state of interest. However, these approaches require a large amount of sample input for accurate analysis

of low-abundance proteins and involve relatively complex and expensive processes. The data analysis is also time-consuming and contributes to low-throughput screening. As such, these candidate biomarkers need to be further verified using multiplex immunoassays, which provide quantitative analysis and adequate sample throughput to meet requirements for statistical significance (Rifai et al., 2006). Increasingly, this validation step is requiring more sensitive measurement of low-abundance biomarkers, which conventional Luminex xMAP and antibody microarrays have difficulty achieving due to lower sensitivity compared to the gold-standard single-plex enzyme linked immunosorbent assay (ELISA). Repeatability and standardization between laboratories are concerns as well (Tighe et al., 2013; Ellington et al., 2010).

To address this gap, numerous technologies have emerged for the

^{*} Corresponding author. Department of Mechanical and Aerospace Engineering, New York University, 6 Metro Tech Center, Brooklyn, NY, 11201, USA. *E-mail address:* kk5165@nyu.edu (K. Kurabayashi).

sensitive and multiplex detection of proteins (Cohen and Walt, 2019; Ren et al., 2021), with single-molecule counting "digital ELISA" demonstrating up to 1000-fold improvement in sensitvity over conventional ELISA (Duffy, 2023). Digital ELISA is achieved by the isolation and detection of single protein molecules on antibody-coated microbeads confined in fL-nL microwells or droplets. Measuring multiple analytes in a single run (multiplexing) is commonly enabled by dye-encoded microbeads (Rissin et al., 2013). Due to the binary nature of digital ELISA, Poisson statistical theory dictates that a minimum number of microbeads must be analyzed to ensure an acceptable theoretical noise level per analyte (Zhang and Noji, 2017). A common approach to signal readout in digital ELISA is to load a suspension of microbeads into microwell arrays by gravity, but this stochastic process can leave more than 30-50% of microwells empty. Multiplexing in digital ELISA therefore requires more beads to be analyzed in an individual microwell array and is limited by this gravity-loading process. Accordingly, increasing the bead loading efficiency has been an active area of research. Improving on the original optical fiber-based digital ELISA by Rissin et al. (2010), Noji and coworkers demonstrated that the background signal of a digital bioassay can be reduced by interrogating a large number of microwells (Kim et al., 2012). The Lammertyn group has shown that bead loading efficiency can be improved by using digital microfluidics to actuate a droplet containing suspended magnetic beads back and forth over hydrophilic microwells while a magnet pulls beads into the microwells (Witters et al., 2013). More recently, they have demonstrated improved loading efficiency using passive hydrophobic surfaces with hydrophilic microwells fabricated using scalable methods (Tripodi et al., 2018; Zandi Shafagh et al., 2019). Quanterix Corp. has demonstrated improved assay performance by tuning the total number of beads used in the reaction combined with a magnetic-meniscus sweeping strategy to assist bead loading (Kan et al., 2020). Our group has recently demonstrated a hybrid spatial-spectral multiplex encoding strategy by pre-seeding the microwell arrays with beads rather than mixing them with the sample solution, allowing multiplexing for up to 14 cytokines (Song et al., 2021a; 2021b; 2021c). Despite these improvements, the total multiplex capacity for bead-based digital ELISA remains limited spectrally by the finite number of flurophores available to encode beads, and spatially by the fixed size of microwell arrays.

Here we introduce a compact, entirely spatially encoded multiplex digital ELISA platform called the "Digital Protein Microarray" (DPMA). Using photolithography, we have developed a novel method of protein patterning that is capable of selectively coating microwell arrays with capture antibodies, eliminating the use of microbeads from the assay and achieving 100% microwell utilization. With precise control of the microwell number, we demonstrate that the sensor area can be miniaturized to a standard 75x25 mm form factor to minimize sample volume consumption. Much like a conventional antibody array, spatial mutliplex encoding is achieved by dispensing capture antibodies in specific microwell areas on the chip, enabling a very high potential multiplex capacity. Numerous practical benefits over our previous platform are realized as well, including the elimination of a bead-counting image analysis step and sensor cross-talk due to bead migration, which enable new, integrative microfluidics applications like our recently described tissue-on-chip platform (Su et al., 2023). Here, the utility of DPMA for biomarker discovery is demonstrated by measuring six serum secretory factors related to glioma tumor progression in a cohort of mice at two different time points. By combining high multiplex capacity, small sample consumption, and sensitivity, the DPMA platform holds great potential to bridge the technical gap between untargeted analyte screening and precise, quantitative, high throughput biomarker validation.

2. Material and methods

2.1. Materials

We purchased 100 mm fused silica wafers from University Wafer Inc, Boston, MA, and positive photoresist MEGAPOSITTM SPRTM220 from Dow Chemical, USA. We obtained (3-Aminopropyl)triethoxysilane (APTES) from Millipore Sigma, St. Louis, MO. We purchased Alexa FlourTM 488 (AF488) goat anti-rat IgG, mouse IL-6, and TNF-α capture and biotinylated detection antibody pairs from BioLegend and LCN2, IFN-γ, CXCL-12, and G-CSF DuoSET ELISA kits from R&D Systems. We purchased the LuminexTM kit from R&D Systems. We obtained avidin-HRP, QuantaRedTM enhanced chemifluorescent HRP substrate, bovine serum albumin (BSA), Casein blocking buffer, and PBS SuperBlock blocking buffer from Thermo Fisher Scientific. We obtained phosphate buffered saline (PBS) from GibcoTM, SylgardTM 184 clear polydimethylsiloxane (PDMS) from Dow Corning, and fluorocarbon HFE oil (NovecTM 7500) from 3MTM.

2.2. Fabrication of glass microwell arrays

Fused silica wafers were first cleaned in piranha solution (3: 1 v/v H_2SO_4 : H_2O_2) and spin-coated with positive photoresist at 3500 RPM to a thickness of 3 μm . Contact-mode photolithography (KARL SÜSS MA/BA6) was used to define arrays of microwells 2.5 μm in diameter arranged in a hexagonal lattice with center-to-center pitch 4 - 20 μm , depending on the experiment (Fig. 2A, step 1). Microwell features were then etched into the fused silica wafer to a depth of 3.5 μm using deep glass reactive ion etching (DGRIE, $\sim\!2500$ Å min $^{-1}$ etch rate, Advanced Plasma System, SPTS) (Fig. 2A, step 2). DPMA chips were finally cut from the fused silica wafers to a form factor of 75x25 mm using a dicing saw (ADT 7100, Advanced Dicing Technologies, Israel) and stored until use.

2.3. Selective surface silanization

With the photoresist in-tact from the microfabrication process, DPMA chips were treated with O2 plasma (50 W, 100% O2, 0.7 Torr, 60 s, Covance, Femto Science, South Korea) to create surface hydroxyl groups inside of the glass microwells. Then, APTES was grafted inside of microwells by chemical vapor deposition (CVD) by placing DPMA chips in a vacuum chamber containing a $\sim\!100~\mu\text{L}$ of liquid APTES at 75 °C for 3 h (Fig. 2A, step 3). DPMA chips were then removed from the vacuum chamber and sonicated in acetone for 5 min and isopropyl alcohol for 5 min to completely remove the photoresist. Rain-XTM was then applied liberally over the surface of the microwell arrays following the manufacturer's instructions (Fig. 2A, step 4). Deionized water contact angle measurements of APTES regions and Rain-XTM-treated regions were obtained using the sessile drop method on a goniometer (DSA100E, KRÜSS GmbH) and fitting the drop shape by the Young-Laplace method (Fig. 2B).

2.4. Coating and visualization of capture antibody in microwells

Capture antibodies were dispensed over microwell surfaces using a handheld micropipette and allowed to incubate overnight at room temperature (Fig. 2D, steps 1-2). Unbound capture antibodies were removed by washing DPMA chips with PBS with 0.1% Tween-20 (PBST). To ensure complete removal of unbound capture antibodies, low residue tape was placed over the microwell arrays and then peeled off (Fig. 2D, step 3). Acrylic flow cells were then affixed over microwell arrays with double-sided tape and filled with SuperBlock blocking buffer for 1 h, followed by Casein blocking buffer for an additional hour. To verify the capture antibody coating (Fig. 2E and F), AF488 goat anti-rat IgG was diluted in PBS, injected into a flow cell, and allowed to incubate for 1 h. The AF488 antibody solution was then washed out of the channel with

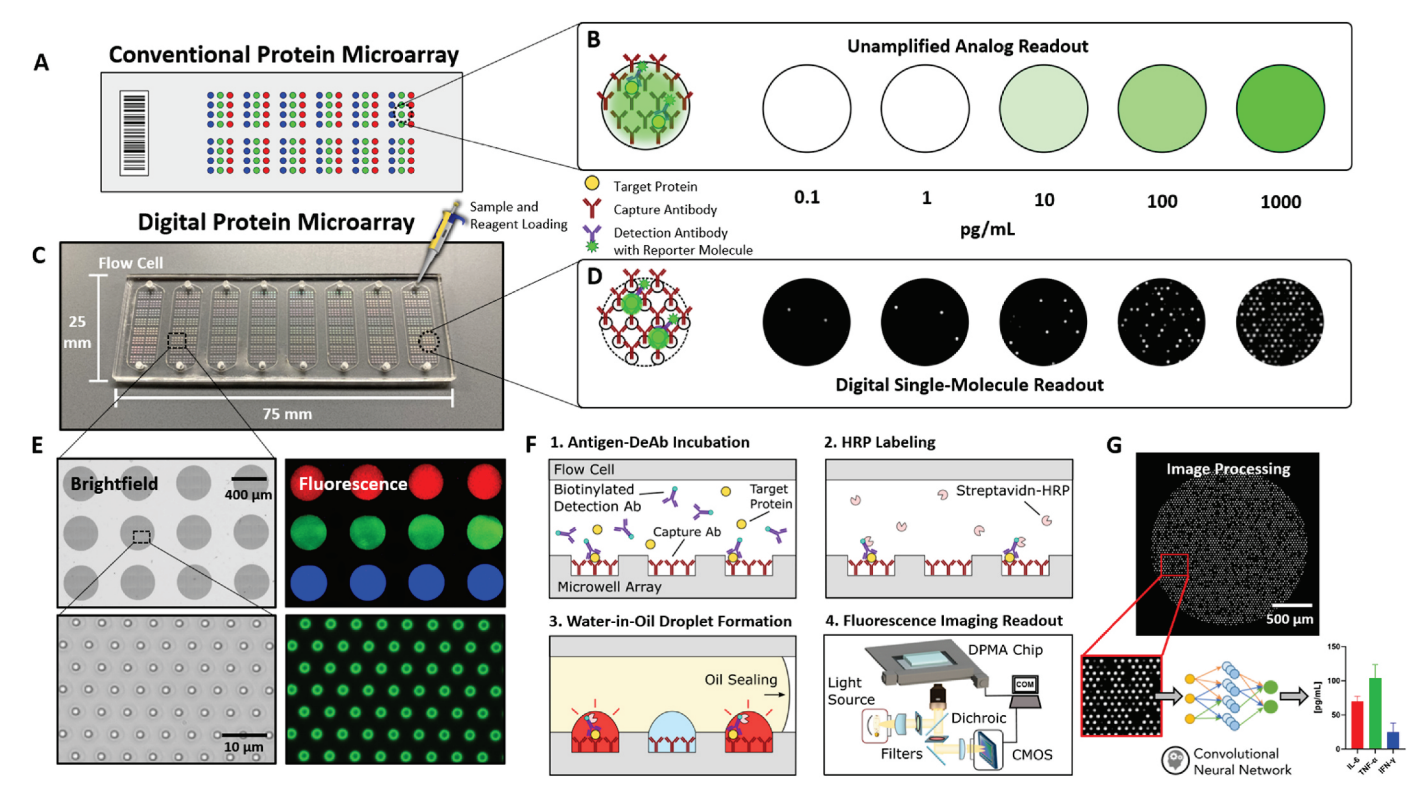


Fig. 1. Digital Protein Microarray (A) Conventional protein microarray schematic. Spots of capture antibodies are printed in addressable locations corresponding to the biomarker being detected. Colors in the schematic refer to a certain biomarker and four replicates are shown. (B) Schematic of the conventional protein microarray detection approach. Target proteins (yellow circles) bind to spots of capture antibody on the substrate (red). Secondary detection antibodies (purple) with a reporter molecule (green star) are used to label the captured analyte molecules. The optical signal (green) diffuses to the bulk medium. The intensity of the optical signal is used to determine the analyte concentration by interpolating from a standard curve. (C) DPMA device fabricated on a standard 75x25 mm form factor glass substrate. An acrylic flow cell is attached over each sensor array to facilitate sample and reagent loading. Holes (top and bottom) are drilled at each end of the flow cell to serve as inlets and outlets. (D) Schematic of single-molecule detection approach used in DPMA. Spots of capture antibody (red) are sub-divided into thousands of microwells (small circles). The individual antibodies shown are a simplified schematic representation of the antibody coating in each microwell. After target protein (yellow circles) capture and labeling with detection antibody (purple) the optical signal (green) is confined within each microwell. Fluorescently-active microwells can be individually counted and the analyte concentration interpolated from a standard curve with improved assay sensitivity (right). (E) Antibodycoated microwell structures in DPMA. Left: Brightfield microscope image of microwell array sensors at 5x magnification (top) and 60x magnification showing individual microwells (bottom). Right: Composite fluorescence image demonstrating multiplex functionalization of microwell arrays. Each row of microwell arrays has been functionalized with a different fluorescently labeled antibody, demonstrating a 3-plex measurement with 4 technical replicates in a single image. Bottom: Green fluorescence channel image of microwells shown in bottom-right. Antibody-coated microwells appear bright green while uncoated regions appear dark. (F) Assay process flow of digital ELISA in DPMA. Panel 1: Sample containingtarget protein (yellow circles) is mixed with a biotinylated detection antibody (purple) in the flow cell over microwell array sensors (gray, bottom). Panel 2: The flow cell is flushed with washing buffer, then a buffer containing streptavidin-HRP is injected into the flow cell to label the antibody-analyte immunocomplexes. Panel 3: The flow cell is washed again, then the HRP substrate is injected into the flow cell (blue), followed by HFE oil (light yellow) to form water-in-oil droplets. The resulting chemiluminescent enzyme product (bright red) is confined within the droplet to reach a detectable concentration by the optical scanner. Panel 4: DPMA chips are imaged using epifluorescence microscopy and an automated X-Y-Z stage. (G) Representative image of microwell array sensor readout. Wells containing analyte molecules appear as bright white spots on the microscope image. Each bright spot is counted by a convolutional neural network programed in MATLAB. The number of bright spots is used to quantify the analyte concentration in the sample. Bar chart shown is representative of data from a 3-plex measurement.

PBST. Confocal images of the microwells (Fig. 3A) were taken using an oil immersion Plan-Apochromat $100 \times /1.35$ NA objective on an inverted microscope (Olympus IX-81) equipped with an iXON3 EMCCD camera (Andor Technology), OBIS lasers (Coherent) with a USB 6003 data acquisition device (National Instruments), and a Yokogawa CSU-X1 spinning disk confocal. Acquisition of images was controlled by Meta-Morph (Molecular Devices). Z-stack images were captured with 488 nm excitation at exposure time of 200 ms. 3D z-projected images were produced by brightest point projection of z stack image sequences in ImageJ.

2.5. Glioma mouse models

2.5.1. Cell line and cell culture conditions

The glioma cells [NPA: shp53, NRAS, shATRX (wt-IDH1); NPAI: shp53, NRAS, shATRX, IDH1-R132H (mIDH1)] were developed in house

de novo by genetically engineering mouse models and isolating the tumor cells for growth in vitro. These glioma cells also harbor luciferase used for in vivo imaging of the tumor. The method for the glioma cell generation is described previously in detail (Alghamri et al., 2021b).

Glioma cells were grown in Dulbecco's Modified Eagle Medium/Nutrient Mixture F-12 (DMEM/F-12) (Gibco, 11320032) supplemented with L-glutamine (Gibco, 25030081), B-27 supplement (Gibco, 17504044), N-2 supplement (Gibco, 17502048), Antibiotic-Antimycotic (Gibco, 15240062), and Normocin (Invivogen, ant-nr-2). Cells were maintained in a humidified incubator at 95% air/5% CO2 (37 °C) and passaged every 3–5 days.

2.5.2. Animal details

Six to eight-week-old female C57BL/6 mice were acquired from Jackson Laboratory. All mice were housed in a pathogen free environment in the University of Michigan vivarium. All studies involving live

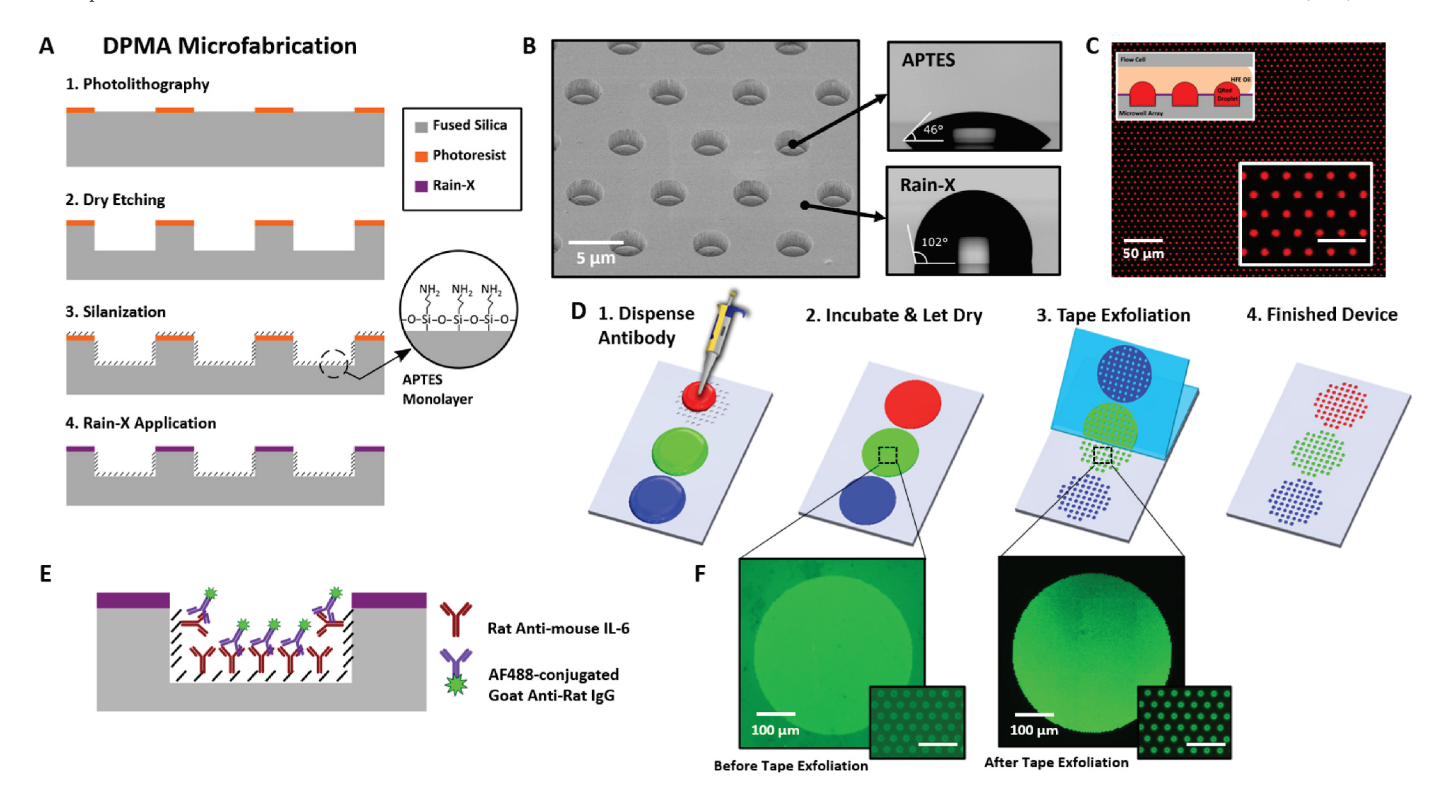


Fig. 2. Fabrication and antibody functionalization of DPMA. (A) Cross-sectional microfabrication diagram (top-to-bottom) of microwell arrays. Step 1: Lithographic patterning of microwell arrays in positive photoresist. Step 2: Dry etching of microwells into a fused silica wafer. Step 3: Silanization of APTES within microwells using chemical vapor deposition. The chemical structure and orientation of APTES is shown in the circular inset figure. Step 4: Photoresist is removed and Rain-XTM is applied to create a hydrophobic surface outside of the microwells. (B) Hydrophilic-in-hydrophobic microwell array surface after microfabrication steps have been completed. Left: Scanning electron microscope (SEM) image taken at 45° perspective of microwell array. Right: Water contact angle measurement of APTES (top) and Rain-XTM (bottom) treated regions of a glass substrate. The recessed microwell surfaces are coated with APTES and are hydrophilic while the rest of the surface is coated with Rain-XTM and is hydrophobic. (C) Verification of water-in-oil droplet formation. A finished DPMA device was flushed with enzyme-converted QuantaRed HRP substrate (resorufin) and then with HFE oil (inset schematic, upper-left). Droplets of QuantaRed appear bright red red while other regions remain dark, indicating confinement of the QuantaRed within microwells. Detail is shown in inset figure (bottom-right), scale bar is 15 μm. (D) Process flow of antibody functionalization (left-to-right). Step 1: Antibodies in coating buffer are dispensed on microwell array surfaces. Step 2: Antibody solution is allowed to incubate and dry. Step 3: Nonspecifically adsorbed antibody on the surface outside of the microwells is removed using the tape exfoliation method. Step 4: Antibody-functionalized devices are ready for use. (E) Assay schematic used to visualize capture antibody coating and verify specificity of patterning within microwells. Microwells were coated with an anti-mouse IL-6 antibody from rat host species and labeled with AF488-conjug

mine were performed in accordance with the Institutional Animal Care & Use Committee (IACUC) at the University of Michigan.

2.5.3. Glioma mouse models and serum collection

Tumor implantation was done as described before (Alghamri et al., 2021b). Briefly, mice are anesthetized using ketamine and dexmedetomidine prior to stereotactic implantation with 50,000 glioma cells in the right striatum. The coordinates for implantation are 0.5 mm anterior and 2.0 mm lateral from the bregma and 3.0 mm ventral from the dura. Glioma cells were injected at a rate of 1 µL/min. A combination of buprenorphine (0.1 mg/kg) and carprofen (5 mg/kg) was administered for analgesia. Carprofen was administered one day post-implantation as well for analgesia. For serum collection, the glioma mouse models were bled at a mid-stage symptomatic time point (day 13 post implantation) and at the time of euthanasia. The mid-stage symptomatic bleed of 0.1 mL to 0.2 mL was done via submandibular bleed (5 mm Goldenrod animal lancet, MEDIpoint). The late-stage symptomatic bleed was done by decapitation after isoflurane overdose. The blood was left to clot in serum collection tubes (Sarstedt, 50-809-211) for 45 min at room temperature. The blood is then centrifuged at 2000×g for 15 min (4 °C) to isolate the serum. Serum samples were stored at -80 $^{\circ}$ C.

Representative images of the glioma progression in vivo were taken using the IVIS Spectrum in vivo imaging system (Fig. 4B) (PerkinElmer, 124262). In brief, $100 \, \mu L$ of luciferin solution was injected 5 min prior to

imaging. During the 5 min, mice were anesthetized with oxygen and isoflurane (2.5% isoflurane), followed by loading mice in the IVIS Spectrum device and imaging. On the connected computer, the Living Imaging software (PerkinElmer) was used to select the region of interest (ROI) as a circle over the head, and bioluminescence intensity was measured.

2.6. Digital ELISA assay

All reagents were prepared in low retention tubes and kept on ice until use. Serum samples and standards were diluted in 50% FBS in Assay Buffer B from Biolegend. Serum samples of 1-10 μL in volume, depending on the dilution factor required, were diluted to a final volume of 30 μL . Standards were created by 5-fold serial dilution in excess volume. Biotinylated detection antibodies were diluted to the working concentration in Assay Buffer B. For multiplex assays, a detection antibody cocktail was created by mixing all detection antibodies together in Assay Buffer B at the required working concentrations. Avidin-HRP was diluted in SuperBlock blocking buffer. Prior to beginning the assay, blocking buffer was washed out of DPMA chips with PBST. For the first assay step, 28 μL of sample or standard was loaded into DPMA chips and mixed in-channel for 15 min (single-plex IL-6, Fig. 3) or 2 h (six-plex assay, Fig. 4) using an automated multichannel pipette system previously described (Song et al., 2021a) to facilitate advective mass

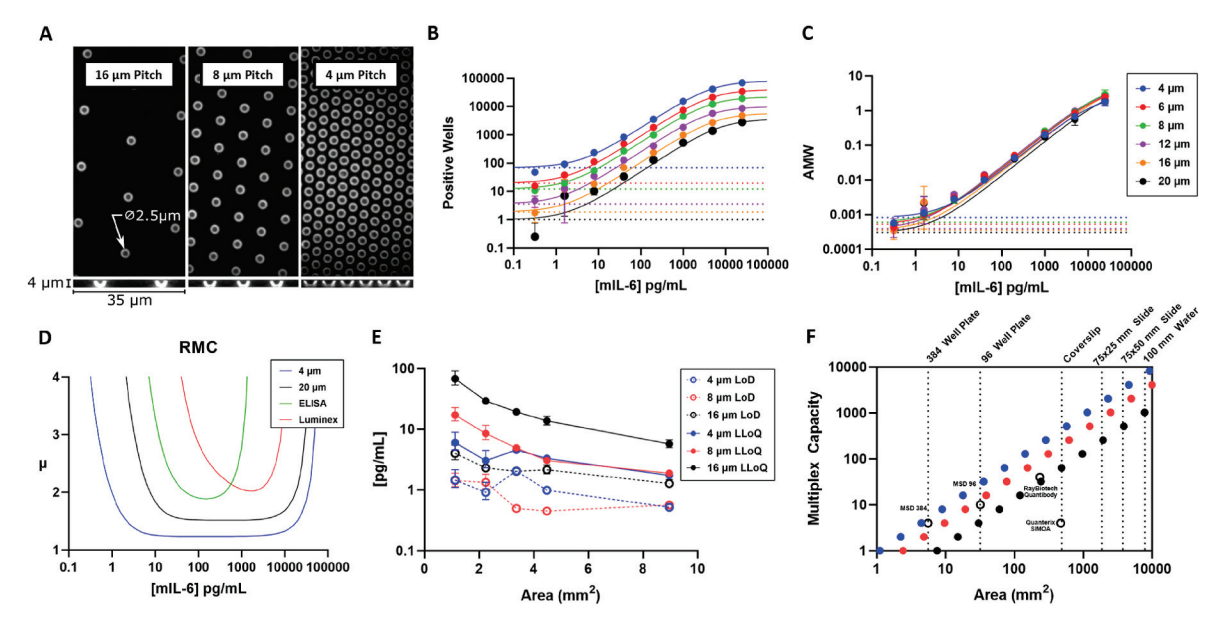


Fig. 3. Photolithographic protein patterning enables miniaturization of digital ELISA. (A) Confocal fluorescence microscope images of microwell arrays of 16, 8, and 4 μm well-to-well pitch (left to right). Top: maximum intensity z-stack projection. Bottom: Z-stack profile taken from a representative cross section, enlarged to show detail. (B-C) Standard curves for microwell arrays of well-to-well pitch 4-20 μm. Each data point is the average of 3 measurements, error bars are one standard of deviation above or below the mean. (D) Resolution of molecular concentration (RMC) versus concentration for 4 μm, 20 μm, and commercial ELISA and Luminex mouse IL-6 kits. The parameter μ indicates the fold difference of analyte concentration that could be resolved with 90% confidence. (E) LoD and LLoQ as total sensor area is increased. (F) Maximum possible sensors versus substrate area for 4 (blue), 8 (red), and 16 (black) μm microwell pitches benchmarked against commercial microarray technologies (empty circles). Dotted lines indicate substrate sizes relevant to various life sciences applications.

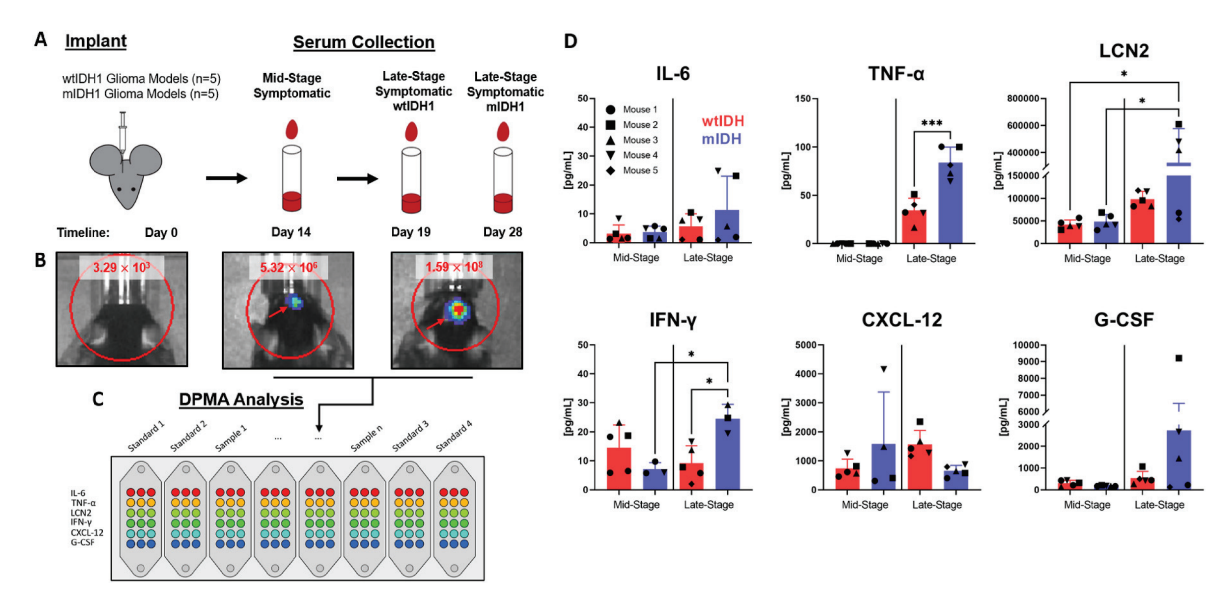


Fig. 4. Application of DPMA in glioma mouse model serum biomarker analysis. (A) Experimental design. Wildtype (wtIDH1) or mutant (mIDH1) glioma cells were implanted in two cohorts of mice on Day 0. Blood serum samples were collected 14 days post-implantation at the "Mid Stage" condition. "Late Stage" blood collection was performed on 19 days (wtIDH1) or 28 days (mIDH1) post-implantation, as mIDH1 tumor harboring mice survive longer than their wildtype counterpart. (B) Example in-vivo imaging system (IVIS) images showing bioluminescent tumors in mice bearing no tumor, mid-stage, and late-stage tumors (indicated by the red arrows). The number in red indicates the bioluminescence signal intensity of the region of interest (ROI) in the red circle (C) Schematic of DPMA used in this study. Microwell arrays were arranged in a grid, with each row addressed to the biomarker being detected. Three duplicate microarrays for each marker allowed for statistical analysis. Flow cells were affixed on top of each microwell array set to allow for up to 10 samples to be run in parallel. (D) Serum biomarker measurements by DPMA. Each data point corresponds to the serum level of an individual mouse in the wildtype or mutant group. Bars are the group mean, error bars are one standard deviation of the group mean, and significance is calculated from group mean. $^*P < 0.05$, $^*P < 0.005$, $^*P < 0.001$. ANOVA. Measurements below the assay LoD were excluded from analysis. Data points below LoD for TNF- α are plotted at 0 pg/mL.

transport to the sensor surface. DPMA chips were then washed by flushing the channels with PBST using a separate automated syringe pump for 2 min at $50 \, \mu L/min$. Using the automated multichannel pipette system again, $28 \, \mu L$ of detection antibody cocktail was loaded onto the

DPMA chips, mixed for 10 min, and washed using the same procedure (Fig. 1F, step 1). Next, 40 μ L of avidin-HRP solution was slowly loaded into DPMA chips for 1 min, then washed with PBST for 10 min (Fig. 1F, step 2). Finally, 35 μ L of QuantaRed substrate solution was manually

loaded into DPMA chips and then flushed with 45 μ L of HFE-7500 oil (Fig. 1F, step 3). DPMA chips were allowed to incubate for 10 min to ensure sufficient concentration of fluorescent enzyme product within the water-in-oil microdroplets could be achieved for single-molecule counting. DPMA chips were then loaded onto an automated fluorescence microscope imaging system consisting of an inverted epifluorescence microscope (Nikon Eclipse Ti) and programmable X-Y-Z motorized stage (ProScan III, Prior Scientific) (Fig. 1F, step 4) (Fig. S1). The stage was controlled by a computer running a custom LabVIEW program that facilitated autofocusing and imaging of microwell arrays at positions pre-defined in the program (Fig. S1). Microwell array images were collected by a $10\times$ microscope objective (Nikon) and CMOS camera (XIMEA xiC) and saved locally on the computer.

2.7. Image and data analysis

Images collected by the imaging system were later analyzed using a previously developed convolutional neural network (CNN) algorithm written in MATLAB (Song et al., 2021c). The CNN was pretrained to recognize and count enzyme active "On" microwells (positive wells) while masking out any defects or contaminations on the microwell array surface. The data produced by the MATLAB-based CNN algorithm was analyzed using GraphPad Prism. Standard curves were fit using the built-in Langmuir adsorption model "One site - Total" and setting the linear nonspecific component to zero. To determine mouse serum biomarker concentrations (Fig. 4), positive wells values were interpolated from a 6-plex standard curve run in parallel on each DPMA device used. Limit of detection (LoD) was calculated as the average background signal plus 3 times the standard deviation (Table 1, "LoD 3 \times σ " column). Lower limit of quantification (LLoQ) was determined by interpolating the signal corresponding to 100 positive wells (Table 1, "LLoQ Poisson" column) or the signal corresponding to the mean plus ten times the background standard deviation (Table 1, "LLoQ $10 \times \sigma$ " column). Resolution of molecular concentration was determined by inputting the standard curve fit parameters calculated by Prism into a Mathematica script made publicly available by Wilson et al. (2022).

3. Results and discussion

3.1. Digital Protein Microarray (DPMA)

Fig. 1 shows the working principle of the Digital Protein Microarray (DPMA) platform. DPMA employs single-molecule counting as a signal amplification strategy to significantly enhance assay sensitivity over conventional protein microarrays. Conventional protein microarrays are manufactured by spotting capture antibodies in a spatially addressable manner on a substrate, commonly at glass slide (Fig. 1A). Samples are then incubated on the substrate in reservoirs, then labeled with a

fluorescent or chemiluminescent secondary antibody. The signal is then read out by a microarray scanner and the fluorescence intensity of each capture antibody spot can be used to determine the analyte concentration. This detection strategy is inherently limited in sensitivity because it lacks an amplification method, such as catalytic turnover by an enzyme as in traditional ELISA. While this limits its quantitative capabilities, the microarray format allows for very high numbers of analyte molecules to be screened while consuming very little sample. In DPMA (Fig. 1C), we have achieved signal amplification by splitting capture antibody spots into hundreds of thousands of femtolieter (fL) microwells (Fig. 1E) in which digital ELISA can be carried out. This new assay format for digital ELISA preserves the very high multiplexing capabilities of the traditional protein microarray, with analytical performance we will show exceeding sub-pg/mL.

The assay procedure is similar to our group's previous work (Song et al., 2021a; 2021b; 2021c). To achieve single-molecule ELISA, an acrylic flow cell can be fixed on top of the DPMA (Fig. 1C) to guide samples and reagents over the microwell array sensors. Antigen capture and labeling is performed with conventional sandwich ELISA chemistry (Fig. 1F, Panel 1-2), further details are provided in the Fig. 1 caption and Material and Methods, Section 2.6. The sample and detection antibody loading volume (25 µL) was enough to completely displace the volume of the flow cell (13 µL). The washing volume used was sufficient for at least 10x replacement of the flow cell volume which minimized any background signal caused by nonspecific binding. To achieve single-molecule detection, the flow cell is flushed with HRP substrate QuantaRed, then flushed again with HFE oil, forming an array of water-in-oil microdroplets over each well. The fluorogenic enzyme product is confined within each microdroplet, so that sufficient concentration of the fluorophore is maintained to observe the signal from one immune complex (Fig. 1F, Panel 3). Signal readout in DPMA is achieved by epifluorescence microscopy on an automated custom scanner (Fig. 1D, Panel 4). The chip can be imaged using a standard epifluorescence microscope equipped with an automated programmable X-Y-Z stage (Fig. S1). We developed a custom LabVIEW program to automatically drive the chip over the stage and acquire images of each array. This enabled "hands-off" operation and helped control run-to-run imaging consistency.

Images of each microwell array collected by the scanner are analyzed using a previously developed AI-enabled MATLAB program (Fig. 1G), (Song et al., 2021c). The MATLAB program counts each well in a binary fashion as "on" or "off" and masks out any defects or contamination on the surface of microwell arrays. Wells containing an analyte molecule appear as bright fluorescence spots in the image, while wells containing no analyte molecule remain dark. Unlike our previous digital immuno-assay platform and many digital assays, the DPMA does not use microbeads, so there is no need to include an additional image analysis step to count how many beads are captured in the array. This reduces the

Table 1Background signal, LoD, and LLoQ of microwell pitch analyzed by positive wells or AMW.

Microwell Pitch	Positive Wells						Average Molecules Per Well (AMW)					
	Background	σ	CV	$\begin{array}{c} \text{LoD} \\ 3\times\sigma(\text{pg/}\\ \text{mL)} \end{array}$	LLoQ Poisson (pg/ mL)	LLoQ $10 \times \sigma \text{ (pg/mL)}$	Background	σ	CV	$\begin{array}{c} LoD \\ 3\times\sigma(pg/\\ mL) \end{array}$	LLoQ Poisson (pg/mL)	LLoQ $10 \times \sigma \text{ (pg/mL)}$
4 μm	69.2	4.32	0.06	0.61	1.77	2.48	8.28×10^{-4}	5.20 × 10 ⁻⁵	0.06	0.69	2.01	2.82
6 μm	19.5	4.96	0.25	0.78	8.92	5.49	$5.28\times10^{\text{-4}}$	1.32×10^{-4}	0.25	0.92	10.42	6.41
8 μm	12.2	4.21	0.35	0.84	16.1	7.7	$5.99\times10^{\text{-4}}$	2.07×10^{-4}	0.35	1.04	20.07	9.59
12 μm	3.63	1.92	0.53	2.65	38.7	7.66	$3.92\times10^{\text{-4}}$	2.08 × 10 ⁻⁴	0.53	3.03	44.11	8.74
16 μm	1.88	1.36	0.72	3.59	94.95	12.93	$3.59\times10^{\text{-4}}$	2.60×10^{-4}	0.72	4.29	112.91	15.42
20 μm	1.00	0.76	0.76	5.05	209.71	15.61	3.02×10^{-4}	2.28×10^{-4}	0.75	5.76	237.58	17.77

scan time and the number of images needed by half and eliminates potential sources of experimental error arising from miscounting beads, wells double-filled with beads, or debris in microwells resulting in bead false-recognition. Since the number of active microwells remains fixed at 100%, the signal measured from each microwell array can simply be reported as the number of positive microwells, or as "average molecules per well (AMW)" which can be calculated by rearranging for λ in the Poisson distribution (Zhang and Noji, 2017):

$$AMW = \lambda = -\ln (1 - P_{positive})$$

where $P_{positive}$ is the fraction of microwells that are fluorescently active in a particular microwell array. This is analogous to "average enzyme per bead (AEB)", "average immunocomplex per bead (AIB)", or similar figures used by other digital immunoassay technologies. We will demonstrate that the number of positive wells or AMW can be used to calculate the analyte concentration by interpolating from a standard curve.

3.2. Fabrication of DPMA

Specific and high-fidelity patterning of proteins into recessed microwell features at the size scale required for the DPMA device ($<10~\mu m$) is not possible with conventional protein patterning methods such as inkjet printing, pin spotting, or dip-pen nanolithography (Bhatt and Shende, 2022). Therefore, we developed a novel protein patterning method using conventional photolithography and wafer-level microfabrication processes (Fig. 2). These processes facilitate both the microwell array manufacturing and enable precise control of the surface chemistry, which is essential to maintain compatibility with later water-in-oil droplet formation necessary for digital ELISA.

3.2.1. Microfabrication of microwell arrays

Microwell features are first patterned in photoresist on a glass wafer using contact-mode photolithography (Fig. 2A, Step 1). Using photolithography allows for many microwell array designs across a range of sizes, shapes, and densities to be realized. Then, reactive ion etching (RIE) is used to etch the microwells into the glass wafer to a depth of 3.5 µm (Fig. 2A, Step 2) (Fig. S7). After etching, individual DPMA devices containing several microwell arrays were singulated from a wafer using a dicing saw. The entire microfabrication procedure required just one photolithography step and a batch of 8 wafers could be completed within one 8-hour workday by one technician. Two DPMA devices of the size (75x25 mm) used in this work could fit on one 100 mm wafer, so the manufacturing throughput of the microfabrication procedure was 16 DPMA devices per day. DPMA devices could be pre-fabricated in batch and stored until use.

3.2.2. Patterned hydrophilic-in-hydrophobic surface chemistry

Protein patterning into microwells in DPMA is enabled by precise control of the substrate surface chemistry. With the photoresist still intact from the RIE process, DPMA devices were treated with O₂ plasma to form hydroxyl groups on the inner surface of the well. Then, (3-Aminopropyl)triethoxysilane (APTES) was grafted onto the surface inside the microwells by chemical vapor deposition (CVD) (Fig. 2A, Step 3). The photoresist effectively masks both the O₂ plasma hydroxylation process and the silane grafting process, leaving only the microwell surface coated with APTES, while regions outside of the microwells retain their native surface chemistry. After CVD, the photoresist was removed by sonication in acetone and isopropyl alcohol.

Microwell arrays used in digital ELISA must be uniformly hydrophobic on the surface in order facilitate droplet formation during the oil sealing process (Kim et al., 2012), with the optimal configuration being a hydrophilic well recessed in a hydrophobic surface (Tripodi et al., 2018). Materials used for dELISA microwell arrays must also have near-zero autofluorescence to maintain a suffcient signal-to-noise ratio

to distinguish "on" from "off" wells. Numerous hydrophobic, low-autofluorescence materials have been demonstrated for bead-based digital ELISA technologies such as PDMS, CYTOP, Teflon, and cyclic olefin copolymer (COC) (Kan et al., 2012, 2020; Kim et al., 2012; Tripodi et al., 2018; Song et al., 2021b). PDMS and COC are incompatible with the silanization process described because they must be molded by soft lithography or injection molding, respectively. CYTOP and Teflon can be micro-machined but they are expensive and challenging to work with in practice. In order to create a hydrophobic surface in DPMA, the automotive glass water repellant Rain-XTM was applied in liquid form over the entire device surface according to the manufacturer's directions (Fig. 2A, Step 4). The hydrophobic component of Rain- X^{TM} consists primarily of PDMS, while other additives chemically hydroxylate the surface it is applied to, allowing the PDMS molecules to bind covalently to the surface (Di Justo, 2010). We found that APTES blocked the Rain-XTM coating process, as areas coated with APTES remained hydrophilic and capable of binding to antibodies while the rest of the surface was made hydrophobic. The water contact angle of APTES-treated regions of DPMA devices was approximately 46° while Rain-XTM regions were approximately 102° (Fig. 2B). This yielded a desirable hydrophilic-in-hydrophobic (HIH) microwell surface configuration and enabled highly uniform water-in-oil microdroplet formation

3.2.3. Specific protein patterning in microwells

The precisely patterned surface chemistry achieved by our microfabrication process enables highly specific coating of antibodies within the glass microwell arrays. First, a solution of capture antibody in coating buffer is mechanically dispensed onto the microwell array surface and allowed to incubate overnight (Fig. 2D, Step 1-2). Currently this process is performed with a handheld micropipette and future work will explore using a microarray printer to automate this process. Antibodies bind to the amine groups of the APTES molecules and remain permanently fixed (Vashist et al., 2014). DPMA devices are then rinsed in washing buffer and allowed to dry (Fig. 2D, Step 1-2). This initial washing removes most of the nonspecifically bound capture antibody, but a thin layer still remains on the substrate outside of the wells (Fig. 2F). In order to achieve micro-scale resolution of antibody patterning and preserve surface hydrophobicity, the remaining antibodies are removed by "tape exfoliation" (Fig. 2D, Step 3) which consists of applying and quickly peeling off a low residue tape over the entire surface of the DPMA. Finally, an acrylic flow cell is attached with double-sided tape and DPMA devices are then ready for use.

We developed an assay to verify the specificity of the antibody coating (Fig. 2E and F). First, nonspecific binding sites are blocked with a blocking buffer flushed into DPMA devices. Then, AF488 anti-IgG antibody is injected and allowed to bind to the patterned capture antibodies (Fig. 2E). Excess anti-IgG antibody is flushed out with washing buffer, and any region on the DPMA chip with patterned antibody produced a bright fluorescent signal (Fig. 2F). Complete, specific, and uniform coating of microwells was verified by confocal microscopy (Fig. 3A). Capture antibody could be seen on the sides and bottom of the wells (Fig. 3A, bottom), but not on surface regions between wells. The donut-shaped fluorescence profile of the microwells (Fig. 3A, top) arises from the 3D shape of the well - the sides of the well appear brighter because the entire fluorescence signal from the well sidewalls is projected onto the image plane. We also used this assay to confirm the efficacy of the tape exfoliation method by imaging antibodies that had been removed by the tape after it had been peeled off (Fig. S3).

3.3. Increasing microwell density enables sensor miniaturization

In previous bead-based digital ELISA platforms, antibody coated microbeads are settled into microwells by gravity. The fill rate is dependent on the bead concentration and microwell geometry, and varies from device-to-device, increasing the experimental CV. In DPMA,

the partition number can be precisely controlled, inconsistencies related to bead loading are eliminated, and the "fill rate" is fixed at 100%. Furthermore, the microwell geometry is no longer constrained to allow optimal bead loading. Leveraging the precision of photolithography, microwell arrays can be designed in any diameter, density, and total area within the process limits. With this new design flexibility, we evaluated the effect of increasing the partition number per sensor area (microwell density) on the assay performance.

3.3.1. Reduction in Poisson noise

DPMA chips were fabricated with a range of microwell array densities (Fig. 3A). The microwells were arranged in a hexagonal lattice with the well-to-well pitch (lattice constant) describing the density. In this study, we considered microwell arrays with pitch ranging from 4 to 20 μm . The microwell diameter and depth were fixed for each array density at 2.5 μm and 3.5 μm , respectively. Standard curves were generated by serially diluting recombinant mouse IL-6 in 50% fetal bovine serum (FBS) and performing digital ELISA as described in Material and Methods. The data is plotted as the total number of "Positive Wells" and as AMW in Fig. 3B and C and summarized in Table 1.

We found that as microwell density is increased, the number of positive wells that are counted for a given concentration also increases. Here, increasing the microwell density is analogous to achieving higher bead filling rate in bead-based dELISA technologies. Generally in digital ELISA, it is advantageous to count as many positive wells as possible in order to minimize the measurement Poisson noise (Kim et al., 2012). We also found that increasing the microwell density also increased the measurement background. This phenomenon has been reported before, and for other bead-based technologies there has been an optimal number of beads reported for certain high-affinity antibody-antigen pairs (Wu et al., 2022). We observed no such trend over the microwell densities we measured and instead found that while the background signal continues to increase with density, the limit of detection decreases. Because of the reduction Poisson noise, the higher density microwell arrays also had a lower background coefficient of variation (CV), yielding a lower overall limit of detection. The data suggest that this trend might continue if the microwell pitch were reduced further; however, decreasing microwell pitch places additional demands on the optical system used to image the microwell arrays to resolve individual wells, and higher magnification or numerical aperture of the objective lens is required. Microwell arrays with a 4 µm pitch were the practical limit of the optical system used in this work, and this design was selected for subsequent experiments. We could discern no trend between the different microwell densities when the data were analyzed by average molecule per well (AMW). In other words, the spatially averaged "on well" frequency is the same across all microwell densities. This can be explained if we consider the total sensor area as a Langmuir adsorption process. For a given area, there is a certain number of analyte molecules, along with detection antibody-HRP reporter immunocomplexes, that will bind to the surface at equilibrium. Since the curves collapse on each other when spatially averaged, what Fig. 3C shows is that increasing the microwell density only increases the sampling rate at which the molecules on that surface are counted, or the number of partitions in the Poisson process. The background, standard deviation, LoD and LLoQ follow the same trend as Fig. 3B. Therefore, either the total number of positive wells or AMW can be used to calculate analyte concentration for the DPMA. We have quantitatively benchmarked the DPMA platform against our previous platform and other relevant multiplex immunoassay platforms in Table S2.

3.3.2. Improvement to measurement resolution

Many immunoassay applications require determining, with statistical certainty, a difference between two or more measured samples. While digital immunoassays have received broad attention for achieving extremely low limits of detection (LoD), this metric does not completely describe the assay's analytical capabilities in, for example, monitoring

biomarker perturbations over time. Recently, Wilson et al. (2022) have proposed the "resolution of molecular concentration (RMC)" as a new performance metric for immunoassays. RMC can be calculated from curve fitting values and the parameter μ indicates the fold difference between two concentrations that can be measured by the assay within a given confidence interval. In our analysis, we used a confidence interval of 90%. In Fig. 3D, the RMC has also been calculated from the commercial ELISA kit we obtained the mouse IL-6 antibody pairs used in the DPMA fabrication. Data from a Luminex kit is included as well. The portions of the RMC curves below 3, about 10 to 1000 pg/mL for ELISA and 70 to 8000 pg/mL for Luminex approximately correspond to the manufacturer's rated linear ranges, with vertical asymptotes at the approximate LLoD and ULoQ, respectively. Both the lower-density 20 μm pitch and higher-density 4 μm pitch DPMA devices achieve a lower and wider μ value < 3 than the analog assays, confirming not only the improvement to sensitivity that single-molecule counting provides, but also a significant improvement to measurement resolution. Beyond improvement to the limit of detection and reduction in Poisson noise, Fig. 3D demonstrates that increasing the microwell density in DPMA, and the digital assay format broadly, also improves the measurement resolution. To our best knowledge, this is the first time a digital and analog assay have been compared by RMC.

3.3.3. Determination of the minimum microwell array size

We next examined the effect of the total microwell array area (the total number of microwells analyzed) on the limit of detection (LoD) and lower limit of quantification (LLoQ). Multiplexing in DPMA is spatially encoded and each microwell array can be coated with a different capture antibody, meaning that the multiplex capacity is ultimately determined by the total microwell array size. Therefore, it is desirable to minimize the microwell array footprint so that the maximum number of sensors can fit into a given substrate area.

For each microwell density we examined, the LoD and LLoQ are plotted in Fig. 3E. Limit of detection was defined as 3 standard deviations above the mean background signal and the LLoQ as the concentration providing at least 100 on wells (theoretical Poisson CV <20%), or 10 standard deviations above the mean background signal, whichever was greater. We found that for all microwell densities, as area was increased both the LoD and LLoQ appear to exponentially decay to lower values. In the data for the 4 μm microwell pitch, one microwell array in the three that were measured had an aberrantly high background signal which increased the CV but was included in analysis. Improvements to LoD and LLoQ appear to be marginal beyond 4 mm², indicating scanning additional area becomes statistically unnecessary depending on the sensitivity required. Generally, the data in Fig. 3E indicate that the optimum sensor performance can be achieved by minimizing the microwell pitch and maximizing the microwell array area, thereby maximizing the total number of wells interrogated in the measurement, which is in good agreement with Poisson statistical theory.

With the LoD and LLoQ determined for each density, we offer in Fig. 3F the theoretical maximum multiplex capacity for various substate sizes relevant to life sciences applications. The unit area for one sensor was calculated from Fig. 3E as the area with which a given microwell density would yield at least 100 positive wells at 5 pg/mL, which is the lower limit of the manufacturer-rated analytical range of the antibody pairs we used. For the highest microwell density DPMA we fabricated, we determined that approximately 30 could fit in the bottom of a single well of a 96 well plate, for example. This is three times the maximum multiplex capacity of the Mesoscale Diagnostics MULTI-ARRAY platform (10-plex), which is the gold standard technique for sensitive and multiplex detection in 96-well plate format. The DPMA is also not limited by form factor and can readily be fabricated on any substrate size and easily integrated with other microfluidics devices. Recently, we demonstrated an early version of the DPMA for a microfluidic tissue-onchip study (Su et al., 2023).

3.4. Low-volume multiplex cytokine detection in mouse serum

Biomedical research studying the effects of complex processes and diseases, such as aging and cancer, or treatments may involve the use of small animal models, which resemble the biological and behavioral characteristics of larger animals. One downside of small animal models is the limited sample volumes they can provide, restricting the types and number of analyses that can be performed for a single animal. The use of microfluidics in DPMA minimizes the sample volume necessary for a single run, increasing the amount of assays that can be run with a single banked sample. This capability is critical in early-stage research, as it allows for different assay protocols, such as the biomarker panel and dilution factor, to be tested for an application without needing to re-run time consuming and laborious animal experiments. To demonstrate its utility in biomarker discovery and monitoring, we used DPMA to analyze the cytokine levels in the serum of glioma mouse models (Fig. 4A and B). We developed a six-plex panel consisting of interleukin-6 (IL-6), tumor necrosis factor alpha (TNF-α), interferon-gamma (IFN-γ), lipocalin-2 (LCN2), and C-X-C motif chemokine ligand-12 (CXCL-12) as these molecules had altered secretion in mIDH1 conditioned media (Alghamri et al., 2021b). The standard curve and cross reactivity assessment for the panel is provided in Figs. S4 and S5. An ELISA correlation is provided for IL-6 in Fig. S6.

Gliomas are tumors of the central nervous system, primarily brain, which are separated into several types based on histopathological, genetic, and epigenetic features (Louis et al., 2021). The mutational status of isocitrate dehydrogenase 1 (IDH1) is used to identify glioma type, as it influences patient clinical outcome by altering the glioma cell biology and the glioma tumor microenvironment (McClellan et al., 2023). Granulocyte colony-stimulating factor (G-CSF), along with several other molecules, was shown to have increased secretion from mutant IDH1 (mIDH1) glioma cells (Alghamri et al., 2021b). Increased systemic G-CSF leads to altered bone marrow granulopoiesis and a reduction of the inhibitory potential of polymorphonuclear myeloid-derived suppressor cells (PMN-MDSCs), which suggests G-CSF as a potential treatment for wildtype IDH1 (wtIDH1) patients (Alghamri et al., 2021b). Given that altered cytokine levels, like that of G-CSF, may lead to changes in the tumor microenvironment and in the body's systemic immune response, here we applied the DPMA to quantify levels of several secretory factors in mouse serum of wtIDH1 and mIDH1 glioma harboring mouse models. IL-6, TNF- α , and IFN- γ are proinflammatory cytokines associated with anti-tumoral properties in the glioma tumor microenvironment (Alghamri et al., 2021a). LCN2 is a small protein which supports tumorigenesis by increasing cell proliferation and cancer cell metastatic potential (Hsieh et al., 2021). CXCL-12 is a chemokine associated with the chemotaxis of immunosuppressive MDSCs into the glioma tumor (Alghamri et al., 2022). In the blood, all six of these six secretory factors mentioned above lead to altered immune response systemically and changes in trafficking of immune cells to the tumor.

We collected serum from wtIDH1 and mIDH1 glioma mouse models at mid-stage and late-stage time points (Fig. 4A). Similar to that of wildtype and mutant IDH1 harboring glioma patients, mIDH1 glioma mouse models survive longer (median survival: 33 days) than the wtIDH1 glioma mouse models (median survival: 21 days) (Alghamri et al., 2021b), so the late-stage blood was collected from the wtIDH1 and mIDH1 glioma mouse models on days 19 and 28 respectively. Here, we see that late-stage G-CSF in the mIDH1 glioma mouse models' serum is increased compared to that from the wtIDH1 glioma mouse models (Fig. 4D), which is predicted based on previous findings (Alghamri et al., 2021b). The mutation of IDH1 by the glioma cells also correlates with increased TNF-α, increased LCN2, and decreased CXCL12 in the serum of late-stage glioma mouse models (Fig. 4D). These results suggest the mutation of IDH1 in the glioma cells affect the immune response systemically by inducing different migration patterns of MDSCs and increasing the stimulation of immune cells via CXCL12 and TNF-α, respectively. The increased LCN2 is one mechanism, by which, mIDH1

may support tumor progression. No changes in the mid-stage time point are observed between the wtIDH1 and mIDH1 glioma mouse model serum, indicating that the mIDH1-induced changes in serum CXCL12 and TNF- α levels happens later in glioma progression and is thus dependent on tumor burden. This study has broad implications for the use of the DPMA as a biomarker validation tool as well as implicating the need for further investigation of these mIDH1-induced serum cytokine level changes. Notably, CXCL12 signaling has been identified as a potential target for glioblastoma treatment (Alghamri et al., 2022). This study implicates CXCL-12 signaling as a more suitable target for wtIDH1 gliomas than for mIDH1.

4. Conclusion and outlook

We have developed a compact and sensitive microarray-format multiplexed immunoassay that achieves signal amplification by singlemolecule counting. Such a platform is urgently needed for biomarker validation, which is trending quickly toward panels of low-abundance biomarkers correlated to disease states. The simple spatial multiplex encoding strategy and sensor miniaturization of our platform was enabled by photolithographic patterning of proteins within microwell arrays. Without needing to consider optical cross-talk due to overlap of fluorophores, the multiplex capacity of DPMA is only limited by the individual sensor size and the available area on the substrate it is fabricated on. This new manufacturing technology enabled precise control of microwell array size and total microwell number. We evaluated the effect of increasing microwell density on the sensor performance and showed that as microwell density is increased, key sensor performance metrics of LoD, LLoQ, and resolution of molecular concentration improve. We saw no trade-off with these performance metrics at the microwell array sizes and densities we investigated and we expect performance to continue to improve should the microwell arrays be further miniaturized. Further miniaturization is possible using more sophisticated photolithography techniques such as projection, electronbeam, or interference lithography and our future work will explore submicrometer well sizes and pitches.

The chief advantage of miniaturizing digital ELISA is to increase the number of parallel assays that can be run for a limited sample volume. DPMA consumed only a small amount of serum (1-10 $\mu L)$ per measurement, which minimally perturbed our mouse models and allowed us to measure several secretory factors during the survival study demonstrated here. Access to this information enables deeper biological insight into disease progression or treatment effects at earlier phases of research, potentially accelerating the discovery of new biomarkers for complex diseases, such as glioma brain tumors. We envision DPMA as a platform technology that can be used in its current microarray format for high multiplex, high sensitivity proteomics and biomarker discovery applications, or integrated into other microfluidics applications requiring sensitive detection of protein analytes.

CRediT authorship contribution statement

Andrew D. Stephens: Conceptualization, Investigation, Methodology, Writing – original draft. Yujing Song: Conceptualization, Software, Validation. Brandon L. McClellan: Methodology, Investigation, Resources, Writing – review & editing. Shiuan-Haur Su: Investigation. Sonnet Xu: Software. Kevin Chen: Investigation. Maria G. Castro: Conceptualization, Methodology, Funding acquisition, Writing – review & editing, Supervision. Benjamin H. Singer: Conceptualization, Funding acquisition, Writing – review & editing, Supervision. Katsuo Kurabayashi: Conceptualization, Methodology, Funding acquisition, Writing – review & editing, Supervision.

Declaration of competing interest

The authors declare the following financial interests/personal

relationships which may be considered as potential competing interests: A U.S. provisional patent was filed for the assay technology reported in the manuscript under Application No 63/433,911 on December 20, 2022.

Data availability

Data will be made available on request.

Acknowledgements

A.D.S., B.H.S, and K.K. were partially supported by National Institutes of Health (NIH) R61HL154249/R33HL154249. B.H.S. was partially supported by R01AG074968. A.D.S. and K.K. were partially supported by National Science Foundation (NSF) CBET 1931905.

Work in M.G.C.'s lab is supported by NIH grants R01NS122165, R01NS124167, R01NS122536, R21NS123879 as well as the Rogel Cancer Center, Ian's Friends Foundation, Chad Tough Foundation, the Pediatric Brain Tumor Foundation, and the Department of Neurosurgery. B.L.M was supported by the University of Michigan Rackham Merit Fellowship and Research Training in Experimental Immunology training grant T32AI007413.

The authors would like to further acknowledge Dr. Yashar Bashirzadeh of the Liu Lab at the University of Michigan for assistance with confocal imaging, Haobo Zhu of the Energy Transport Lab at the University of Michigan for assistance with water contact angle measurements, and Dr. Brandon Wilson of the Soh Lab at Stanford University for valuable discussions regarding resolution of molecular concentration (RMC) analysis. Device fabrication was performed at the University of Michigan Lurie Nanofabrication Facility.

Appendix A. Supplementary data

Supplementary data to this article can be found online at https://doi.org/10.1016/j.bios.2023.115536.

References

- Alghamri, M.S., McClellan, B.L., Hartlage, C.S., Haase, S., Faisal, S.M., Thalla, R., Dabaja, A., Banerjee, K., Carney, S.V., Mujeeb, A.A., Olin, M.R., Moon, J.J., Schwendeman, A., Lowenstein, P.R., Castro, M.G., 2021a. Targeting neuroinflammation in brain cancer: uncovering mechanisms, pharmacological targets, and neuropharmaceutical developments. Front. Pharmacol. 12, 680021.
- Alghamri, M.S., McClellan, B.L., Avvari, R.P., Thalla, R., Carney, S., Hartlage, C.S., Haase, S., Ventosa, M., Taher, A., Kamran, N., Zhang, L., Faisal, S.M., Núñez, F.J., Garcia-Fabiani, M.B., Al-Holou, W.N., Orringer, D., Hervey-Jumper, S., Heth, J., Patil, P.G., Eddy, K., Merajver, S.D., Ulintz, P.J., Welch, J., Gao, C., Liu, J., Núñez, G., Hambardzumyan, D., Lowenstein, P.R., Castro, M.G., 2021b. G-CSF secreted by mutant IDH1 glioma stem cells abolishes myeloid cell immunosuppression and enhances the efficacy of immunotherapy. Sci. Adv. 7 (40), eabh3243.
- Alghamri, M.S., Banerjee, K., Mujeeb, A.A., Mauser, A., Taher, A., Thalla, R., McClellan, B.L., Varela, M.L., Stamatovic, S.M., Martinez-Revollar, G., Andjelkovic, A.V., Gregory, J.V., Kadiyala, P., Calinescu, A., Jiménez, J.A., Apfelbaum, A.A., Lawlor, E.R., Carney, S., Comba, A., Faisal, S.M., Barissi, M., Edwards, M.B., Appelman, H., Sun, Y., Gan, J., Ackermann, R., Schwendeman, A., Candolfi, M., Olin, M.R., Lahann, J., Lowenstein, P.R., Castro, M.G., 2022. Systemic delivery of an adjuvant CXCR4-CXCL12 signaling inhibitor encapsulated in synthetic protein nanoparticles for glioma immunotherapy. ACS Nano 16 (6), 8729–8750.
- Bhatt, M., Shende, P., 2022. Surface patterning techniques for proteins on nano- and micro-systems: a modulated aspect in hierarchical structures. J. Mater. Chem. B 10 (8), 1176–1195.
- Borrebaeck, C., 2018. Precision diagnostics: moving towards protein biomarker signatures of clinical utility in cancer. Nat. Rev. Cancer 17, 199–204.
- Cohen, L., Walt, D.R., 2019. Highly sensitive and multiplexed protein measurements. Chem. Rev. 119 (1), 293–321.
- Di Justo, P., 2010. What's inside: rain-X. Better driving through alcohol. Wired. https://www.wired.com/2010/06/st-whatsinside-rainx/.
- Duffy, D.C., 2023. Digital detection of proteins. Lab Chip 23 (5), 818–847.
 Ellington, A.A., Kullo, I.J., Bailey, K.R., Klee, G.G., 2010. Antibody-based protein multiplex platforms: technical and operational challenges. Clin. Chem. 56 (2),
- Hsieh, Y.H., Tsai, J.P., Yu, C.L., Lee, C.C., Hsu, J.C., Chen, J.C., 2021. Overexpression of lipocalin-2 inhibits proliferation and invasiveness of human glioblastoma

- multiforme cells by activating ERK targeting cathepsin D expression. Biology 10 (5),
- Kan, C.W., Rivnak, A.J., Campbell, T.G., Piech, T., Rissin, D.M., Mösl, M., Peterça, A., Niederberger, H.P., Minnehan, K.A., Patel, P.P., Ferrell, E.P., Meyer, R.E., Chang, L., Wilson, D.H., Fournier, D.R., Duffy, D.C., 2012. Isolation and detection of single molecules on paramagnetic beads using sequential fluid flows in microfabricated polymer array assemblies. Lab Chip 12 (5), 977–985.
- Kan, C.W., Tobos, C.I., Rissin, D.M., Wiener, A.D., Meyer, R.E., Svancara, D.M., Comperchio, A., Warwick, C., Millington, R., Collier, N., Duffy, D.C., 2020. Digital enzyme-linked immunosorbent assays with sub-attomolar detection limits based on low numbers of capture beads combined with high efficiency bead analysis. Lab Chip 20, 2122–2135.
- Kim, S.H., Iwai, S., Araki, S., Sakakihara, S., Iino, R., Noji, H., 2012. Large-scale femtoliter droplet array for digital counting of single biomolecules. Lab Chip 12 (23), 4986–4991.
- Louis, D.N., Perry, A., Wesseling, P., Brat, D.J., Cree, I.A., Figarella-Branger, D., Hawkins, C., Ng, H.K., Pfister, S.M., Reifenberger, G., Soffietti, R., von Deimling, A., Ellison, D.W., 2021. The 2021 WHO classification of tumors of the central nervous system: a summary. Neuro Oncol. 23 (8), 1231–1251.
- McClellan, B.L., Haase, S., Nunez, F.J., Alghamri, M.S., Dabaja, A.A., Lowenstein, P.R., Castro, M.G., 2023. Impact of epigenetic reprogramming on antitumor immune responses in glioma. J. Clin. Invest. 133 (2), e163450.
- Park, K.C., Gaze, D.C., Collinson, P.O., Marber, M.S., 2017. Cardiac troponins: from myocardial infarction to chronic disease. Cardiovasc. Res. 113 (14), 1708–1718.
- Ren, A.H., Diamandis, E.P., Kulasingam, V., 2021. Uncovering the depths of the human proteome: antibody-based technologies for ultrasensitive multiplexed protein detection and quantification. Mol. Cell. Proteomics 20, 100155.
- Rifai, N., Gillette, M., Carr, S., 2006. Protein biomarker discovery and validation: the long and uncertain path to clinical utility. Nat. Biotechnol. 24, 971–983.
- Rissin, D.M., Kan, C.W., Campbell, T.G., Howes, S.C., Fournier, D.R., Song, L., Piech, T., Patel, P.P., Chang, L., Rivnak, A.J., Ferrell, E.P., Randall, J.D., Provuncher, G.K., Walt, D.R., Duffy, D.C., 2010. Single-molecule enzyme-linked immunosorbent assay detects serum proteins at subfemtomolar concentrations. Nat. Biotechnol. 28 (6), 595–599.
- Rissin, D.M., Kan, C.W., Song, L., Rivnak, A.J., Fishburn, M.W., Shao, Q., Piech, T., Ferrell, E.P., Meyer, R.E., Campbell, T.G., Fournier, D.R., Duffy, D.C., 2013. Multiplexed single molecule immunoassays. Lab Chip 13, 2902–2911.
- Sarma, A., Calfee, C.S., Ware, L.B., 2020. Biomarkers and precision medicine: state of the art. Crit. Care Clin. 36 (1), 155–165.
- Song, Y., Ye, Y., Su, S.H., Stephens, A., Cai, T., Chung, M.T., Han, M.K., Newstead, M.W., Yessayan, L., Frame, D., Humes, H.D., Singer, B.H., Kurabayashi, K., 2021a. A digital protein microarray for COVID-19 cytokine storm monitoring. Lab Chip 21 (2), 331–343.
- Song, Y., Sandford, E., Tian, Y., Yin, Q., Kozminski, A.G., Su, S.H., Cai, T., Ye, Y., Chung, M.T., Lindstrom, R., Goicochea, A., Barabas, J., Olesnavich, M., Rozwadowski, M., Li, Y., Alam, H.B., Singer, B.H., Ghosh, M., Choi, S.W., Tewari, M., Kurabayashi, K., 2021b. Rapid single-molecule digital detection of protein biomarkers for continuous monitoring of systemic immune disorders. Blood 137 (12), 1591–1602.
- Song, Y., Zhao, J., Cai, T., Stephens, A., Su, S.H., Sandford, E., Flora, C., Singer, B.H., Ghosh, M., Choi, S.W., Tewari, M., Kurabayashi, K., 2021c. Machine learning-based cytokine microarray digital immunoassay analysis. Biosens. Bioelectron. 180, 113088
- Su, S.H., Song, Y., Stephens, A., Situ, M., McCloskey, M.C., McGrath, J.L., Andjelkovic, A. V., Singer, B.H., Kurabayashi, K., 2023. A tissue chip with integrated digital immunosensors: in situ brain endothelial barrier cytokine secretion monitoring. Biosens. Bioelectron. 224, 115030.
- Tighe, P., Negm, O., Todd, I., Fairclough, L., 2013. Utility, reliability and reproducibility of immunoassay multiplex kits. Methods 61 (1), 23–29.
- Tripodi, L., Ven, K., Kil, D., Rutten, I., Puers, R., Lammertyn, J., 2018. Teflon-on-Glass molding enables high-throughput fabrication of hydrophilic-in-hydrophobic microwells for bead-based digital bioassays. Materials 11, 2154.
- Vashist, S.K., Lam, E., Hrapovic, S., Male, K.B., Luong, J.H., 2014. Immobilization of antibodies and enzymes on 3-aminopropyltriethoxysilane-functionalized bioanalytical platforms for biosensors and diagnostics. Chem. Rev. 114 (21), 11083–11130.
- Waury, K., Willemse, E.A.J., Vanmechelen, E., Zetterberg, H., Teunissen, C.E., Abeln, S., 2022. Bioinformatics tools and data resources for assay development of fluid protein biomarkers. Biomark. Res. 83 (10).
- Wilson, B.D., Eisenstein, M., Soh, H.T., 2022. Comparing assays via the resolution of molecular concentration. Nat. Biomed. Eng. 6 (3), 227–231.
- Witters, D., Knez, K., Ceyssens, F., Puers, R., Lammertyn, J., 2013. Digital microfluidics-enabled single-molecule detection by printing and sealing single magnetic beads in femtoliter droplets. Lab Chip 13, 2047–2054.
- Wu, C., Dougan, T.J., Walt, D.R., 2022. High-throughput, high-multiplex digital protein detection with attomolar sensitivity. ACS Nano 16 (1), 1025–1035.
- Zandi Shafagh, R., Decrop, D., Ven, K., Vanderbeke, A., Hanusa, R., Breukers, J., Pardon, G., Haraldsson, T., Lammertyn, J., van der Wijngaart, W., 2019. Reaction injection molding of hydrophilic-in-hydrophobic femtolitre-well arrays. Microsyst. Nanoeng. 5, 25.
- Zetterberg, H., Blennow, K., 2020. Blood biomarkers: democratizing alzheimer's diagnostics. Neuron 106 (6), 881–883.
- Zhang, Y., Noji, H., 2017. Digital bioassays: theory, applications, and perspectives. Anal. Chem. 89 (1), 92–101.